

ARTICLE OPEN



The role of upper-ocean variations of the Kuroshio-Oyashio Extension in seasonal-to-decadal air-sea heat flux variability

Youngji Joh¹✉, Thomas L. Delworth², Andrew T. Wittenberg², Xiaosong Yang², Anthony Rosati^{2,3}, Nathaniel C. Johnson² and Liwei Jia^{2,3}

The Kuroshio-Oyashio Extension (KOE) is the North Pacific oceanic frontal zone where air-sea heat and moisture exchanges allow strong communication between the ocean and atmosphere. Using satellite observations and reanalysis datasets, we show that the KOE surface heat flux variations are very closely linked to Kuroshio Extension (KE) sea surface height (SSH) variability on both seasonal and decadal time scales. We investigate seasonal oceanic and atmospheric anomalies associated with anomalous KE upper ocean temperature, as reflected in SSH anomalies (SSHa). We show that the ocean-induced seasonal changes in air-sea coupled processes, which are accompanied by KE upper-ocean temperature anomalies, lead to significant ocean-to-atmosphere heat transfer during November–December–January (i.e., NDJ). This anomalous NDJ KOE upward heat transfer has recently grown stronger in the observational record, which also appears to be associated with the enhanced KE decadal variability. Highlighting the role of KOE heat fluxes as a communicator between the upper-ocean and the overlying atmosphere, our findings suggest that NDJ KOE heat flux variations could be a useful North Pacific climate indicator.

npj Climate and Atmospheric Science (2023)6:123; <https://doi.org/10.1038/s41612-023-00453-9>

INTRODUCTION

The Kuroshio and Oyashio Extension (KOE; Fig. 1a) region is a major part of the North Pacific western boundary current system (WBC), known as the most prominent extratropical coupled ocean-atmosphere system over the North Pacific^{1–4}. As the North Pacific oceanic frontal zone, the KOE region includes strong SST gradients over the Oyashio Extension (OE) and a sharp SSH gradient over the Kuroshio Extension (KE)^{3,5–7}. Many observational and modeling studies have shown that interannual-to-decadal variations of the KOE are accompanied by changes in the position and meridional gradient of the SST and SSH fronts^{2–5,8–18}.

The KE region (31°–36°N, 140°–165°E) is especially characterized by interannual and decadal timescale and large-scale air-sea coupled processes in the midlatitude North Pacific, such as wind-induced oceanic Rossby wave propagations^{5,12,19,20}. The recent KE modulations since 1980 between the positive and negative phase of KE SSH anomalies have preferred decadal time scales^{8,15,21–23}. To be specific, a positive KE phase (e.g., positive KE SSH anomalies, Fig. 1a) is accompanied by an enhanced southern recirculation gyre, stronger KE eastward transport, and a northward-shifted oceanic jet^{9,15}. The detailed description and synthesized schematic can be found in Fig. 1 of Qiu (2019)²⁴. During the positive KE phase, the intensified KE current and eastward jet enhance tropical-origin warm water transport into the KE region and beyond into the midlatitude North Pacific, thereby significantly impacting ocean thermodynamic properties^{5,9}. The reverse holds when the KE transitions to the negative KE SSH phase.

The decadal KE SSH variability is known to be associated with large-scale Pacific climate modes - constituting the Pacific Decadal Oscillation (PDO) and North Pacific Gyre Oscillation^{6,9,14,15,22,25,26}. In addition, observational and modeling studies have suggested that midlatitude KE SSH fluctuations may closely interact with the subtropical and tropical variability like the Pacific Meridional Modes (PMM) and El Niño-Southern Oscillation (ENSO)^{21,27}. Those

studies highlight the KE downstream response as a slow nudging of atmospheric circulation anomalies that can reduce/enhance the trade winds, which are key to driving changes in the subtropical and tropical Pacific variability. Also, other studies have described the KE low-frequency expression as a new mode of quasi-decadal Pacific climate variability named ocean-atmosphere coupled Pacific Decadal Procession^{28,29}. Moreover, a recent study suggests that the North Pacific SSH anomalies, especially along the KE region, may contribute to initiating ocean temperature extremes like Northeast Pacific Marine Heatwaves³⁰. Growing observational evidence suggests that the KE SSH variability could be a crucial climate indicator of extratropical-tropical teleconnections, air-sea coupling, and extreme events, potentially leading to Pacific climate predictability on decadal time scales. However, a fundamental question remains to be clarified - what are the mechanisms and characteristics by which interannual to decadal scale variations of SSH or accompanied anomalies physically impact air-sea fluxes, and how have the seasonal impacts of those strong decadal fluctuations affected the Pacific climate?

In this study, we use KE SSH variability as an indicator of changes in upper-ocean heat content over the Northwestern Pacific^{6,8,18,20,31–35}; many previous studies have shown that on seasonal-to-decadal scales, changes in upper-ocean heat content account for most of the large-scale changes in SSH^{32,33}. As ocean heat content variability is largely governed by temperature over the KE region⁶, we focus on the role of the anomalous upper-ocean temperatures associated with KE SSH variability in driving regional and large-scale air-sea interactions on seasonal-to-decadal time scales (e.g., rather than describing small-scale oceanic processes^{36,37}). We first identify key patterns of surface latent and sensible heat flux anomalies associated with KE SSH anomalies (SSHa). We then investigate seasonal variations in coupled ocean-atmosphere processes, including air-sea heat transfer, due to impacts of upper-ocean temperature anomalies

¹Atmospheric and Oceanic Sciences Program, Princeton University, Princeton, NJ, USA. ²Geophysical Fluid Dynamics Laboratory/NOAA, 201 Forrestal Road, Princeton, NJ, USA. ³University Corporation for Atmospheric Research, Boulder, CO, USA. ✉email: youngji.joh@princeton.edu

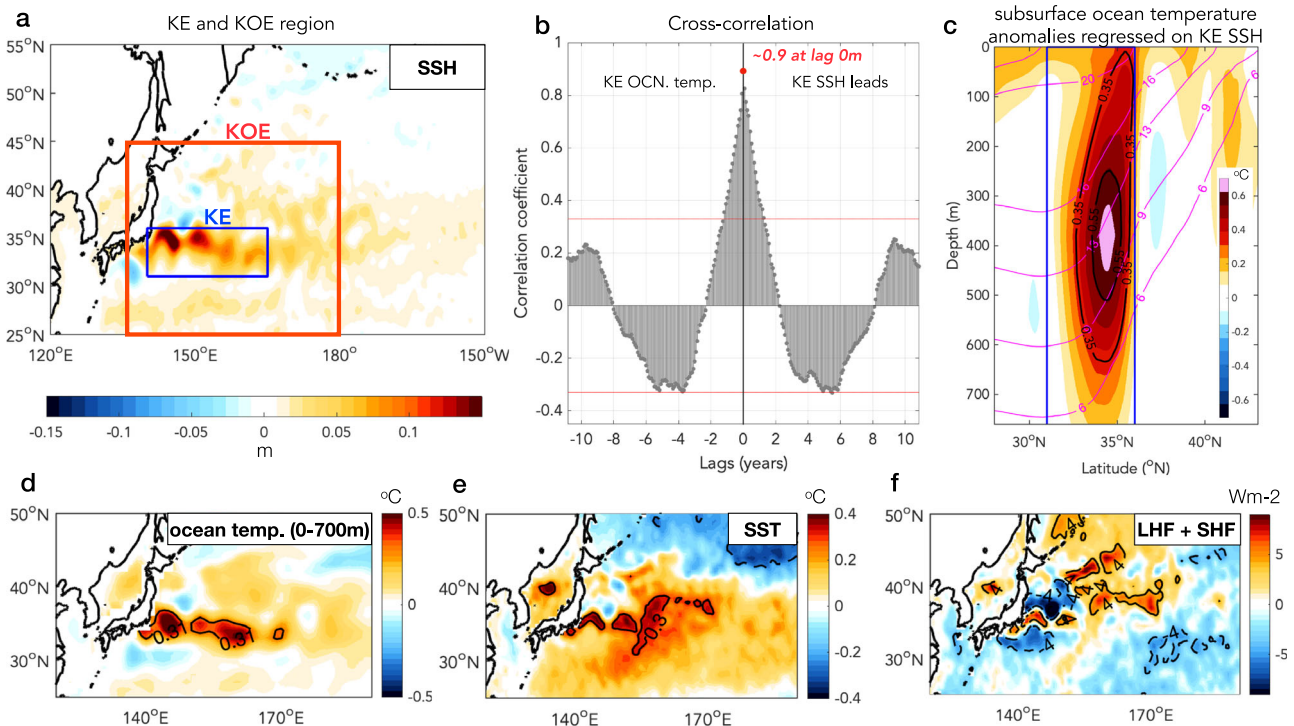


Fig. 1 KE SSH variability as an indicator of ocean heat content. **a** Regression coefficients of SSH anomalies with KE SSH index without lags. The blue and red box each indicate the KE (31° – 36° N, 140° – 165° E) and KOE (25° – 45° N, 135° – 180° E) region used in this study. **b** Cross-correlation function between the KE SSH index and KE ocean temperature for the upper 700-m of the ocean, where those anomalies are averaged over the KE band (31° – 36° N, 140° – 165° E). **c** Depth-latitude map of the regression coefficient between zonal-mean (140° – 165° E) ocean temperature anomalies ($^{\circ}$ C) and the KE SSH index without lags. The mean temperature is shown as magenta contours. **d–f** Spatial maps of the regression coefficient of **(d)**, 0–700 upper ocean temperature ($^{\circ}$ C) **(e)**, SST ($^{\circ}$ C) **(f)**, and sum (Wm^{-2} ; upward positive) of surface LHF and SHF anomalies with the normalized KE SSH index with no lags. Black contours in **c–f** indicate regression coefficients statistically significant at the 10% level. In all panels, the KE SSH index is normalized with dividing by one standard deviation. Monthly indices for period from 1993 to 2022 are used.

on SST and atmospheric circulation and, finally, show how the earlier winter KOE surface heat flux anomalies are closely linked to KE SSH variability on seasonal and decadal time scales.

RESULTS

Decadal KE upper ocean variations

The cross-correlation between the KE SSH and 0–700 m averaged KE ocean temperature (Fig. 1b) shows that KE SSH anomalies are strongly accompanied by upper-ocean thermal anomalies on decadal time scales^{33,38}. These strong decadal variations of subsurface KOE are known to be modulated by basin-scale wind stress curl variability via baroclinic oceanic Rossby wave propagation that induces anomalous thermocline depth and ocean heat content^{5,19,31,39–42}. The sinusoidal shape of the cross-correlation indicates that those oceanic variations have a decadal oscillatory nature, which corresponds to a period of ~9–11 years. Linear regression of zonally-averaged (140° – 165° E) ocean temperature anomalies onto the KE SSH index (Fig. 1c) shows the largest temperature anomalies at the KE band (31° – 36° N), particularly at 300–600 m depth which is near the mean thermocline. Given the significant contributions of temperature anomalies (e.g., larger contributions than salinity) on the ocean heat content variability over the North Pacific WBC region⁶, we interpret the ocean temperature anomalies associated with KE SSH in this study as the upper-ocean heat content accompanied by wind-induced KE SSH changes. Note that in the rest of the paper, we use the normalized KE SSH index, which is divided by one standard deviation, to show typical magnitudes of KE SSH anomalies associated with upper ocean temperature variations. The KOE region is characterized by a strong SST gradient and isotherms that slopes steeply

downward toward the southeast (pink lines in Fig. 1c). Thus, as the latitude of the KOE fluctuates, this region experiences significant seasonal-to-decadal variations in SST, mixed layer depths, and the upper-ocean heat budget^{32,43,44}.

We continue to show and compare surface anomaly patterns associated with KE SSH using regression maps of SSH, depth-averaged ocean temperature, SST, and the sum of the latent surface heat flux (LHF) and sensible surface heat flux (SHF) with respect to the KE SSH index (Fig. 1a and d–f). Those regression maps (with no lags) exhibit that the ocean thermal anomalies (Fig. 1d) show a high correspondence with the SSH anomaly pattern (Fig. 1a) and also with SST (Fig. 1e) and heat flux (Fig. 1f) anomalies. The same sign of ocean temperature, SST, and heat fluxes (upward positive) anomalies, especially over the eastward KE jet, reveals the export of heat from the ocean to the atmosphere, suggesting that those ocean temperature anomalies did not originate from local atmospheric forcing. We note that while anomalous SSH (Fig. 1a) and ocean temperature (Fig. 1d) are characterized by quasi-stationary meander patterns over the 144° E and 150° E⁹, the SST regression (Fig. 1e) shows a rather complex pattern, including a frontal boundary signature (e.g., North-south dipole anomaly pattern) as well as the local KOE anomalies. We later discuss the role of those large-scale dipole SST anomalies resembling the North-South phase pattern (see Supplementary Fig. 1) in seasonal KOE evolutions²², but here we focus on the local KOE anomalies that represent the anomalous oceanic heat content. The surface heat flux regression (Fig. 1f), with positive anomalies over the upstream KE jet and its downstream, indicates that the upward heat fluxes act to damp the warm SST anomalies.

It is important to note that the most prominent response of KOE LHF and SHF anomalies to KE SSH is found when the KE SSH leads

SST, LHF, and SHF anomalies regressed on KE SSH index

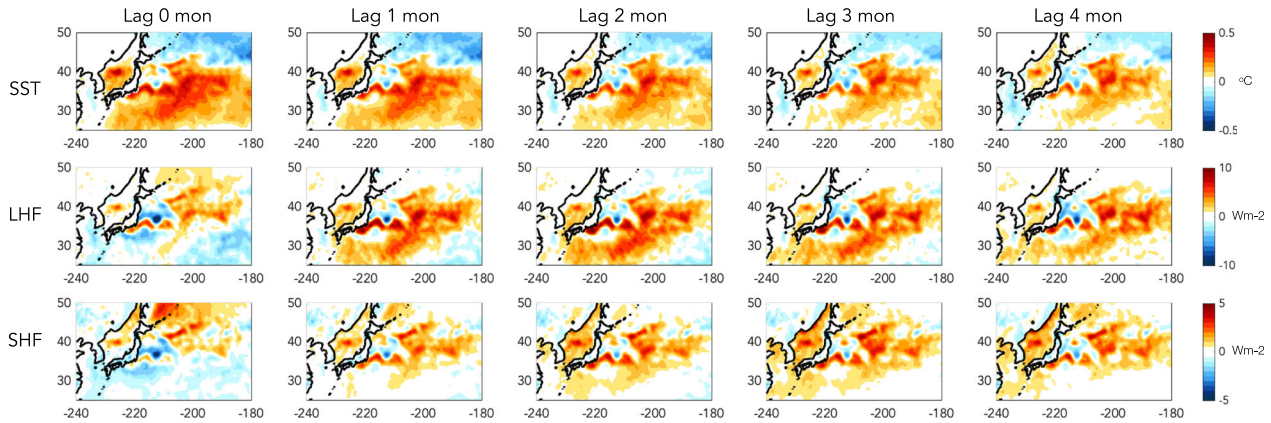


Fig. 2 Evolution of SST, LHF, and SHF anomalies associated with KE SSH on monthly time scales. Lagged regression maps of (top) SST ($^{\circ}\text{C}$), (middle) LHF (upward positive, Wm^{-2}), and (bottom) SHF (upward positive, Wm^{-2}) anomalies onto the normalized KE SSH index, where KE SSH leads the anomalies by 0, 1, 2, and 3 months. In all panels, the KE SSH index is normalized by dividing by one standard deviation. Monthly indices for the period from 1993 to 2022 are used.

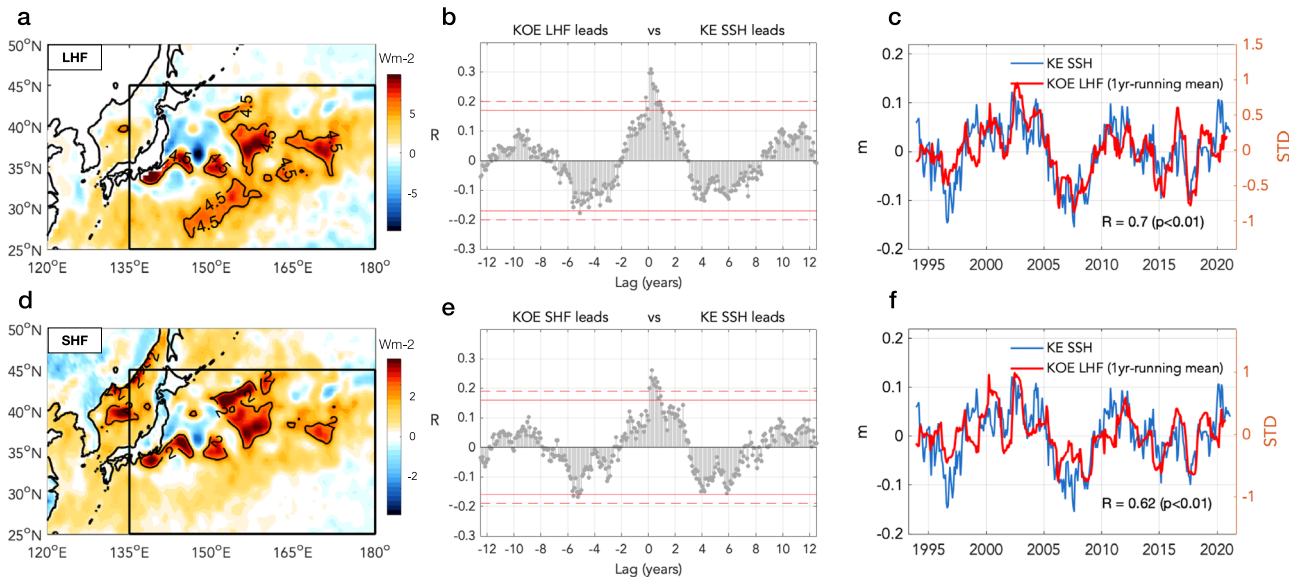


Fig. 3 Decadal covariability between KE SSH and surface KOE LHF/SHF variations. **a** Map of lag-regression coefficients for the linear regression of 3-month-lagged surface LHF anomalies (Wm^{-2}) on the normalized KE SSH index, which is divided by one standard deviation. **b** Cross-correlation function of the monthly KE SSH and KOE LHF indices (no filtering applied). The dashed and solid red lines indicate correlation coefficients statistically significant at the 5% and 10%, respectively, based on a two-sided t -test with the adjusted degrees of freedom. **c** Monthly time series of the KE SSH index (blue) and 1-year running mean KOE LHF (red) with a correlation between the two. **d–f** Same as in (a–c) but for the surface SHF. Note that the SHF amplitude is nearly half of the LHF amplitude (compare **a** and **d**). In **a** and **d**, the black contours indicate regression coefficients statistically significant at the 10% level, and the black box is the domain used for defining the KOE LHF/SHF indices (see methods for details).

heat flux anomalies by 2–4 months, not at lag 0 months (Fig. 2). Given the delayed response of KOE heat fluxes to KE SSH, we focus on the lagged KOE heat flux anomalies associated with KE SSH and use their spatial structures to identify corresponding temporal evolutions in Fig. 3. In Fig. 3a, the 3-month lagged LHF anomalies regressed on the KE SSH index reveal upward heat flux over the upstream region [140° – 153°E], especially the two quasi-stationary meanders, and over the larger downstream region [153° – 165°E]. A cross-correlation function between the KE SSH and KOE LHF timeseries (see methods for details) confirms their strong covariability on decadal time scales (Fig. 3b). The oscillatory character and time scale of KOE LHF and KE SSH are nearly identical to those of KOE oceanic variations shown in Fig. 1b (Note that no filtering is applied to the indices). When a 1-year running

mean is applied to KOE LHF, the correlation between KE SSH and low-pass filtered KOE LHF reaches 0.7 (Fig. 3c), revealing that near half of the low-frequency KOE LHF variability can be explained by upper-ocean dynamics (e.g., KE SSH or KOE ocean temperature anomalies). Analysis of KOE SHF (Fig. 3d–f) shows similar results of LHF (Fig. 3a–c), except that the prominent SHF anomalies are found in the relatively northern KOE region poleward of 42°N (Fig. 3d).

Seasonal KE variations and associated air-sea coupled processes

To investigate seasonal variations of KE upper-ocean variability, we first examine seasonal changes in ocean temperature anomalies associated with KE SSH and their impacts on air-sea coupled

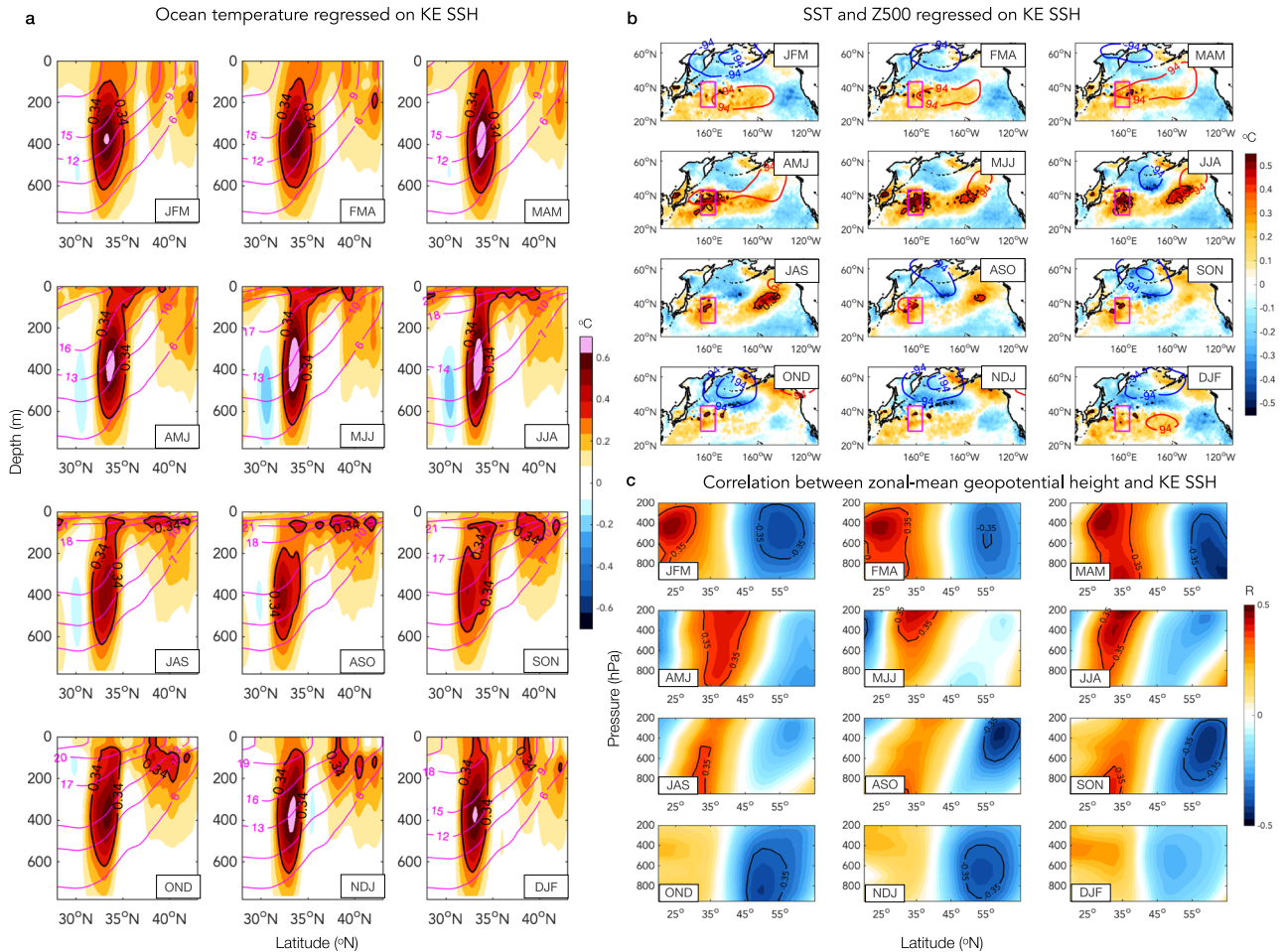


Fig. 4 Seasonal impacts of upper ocean variability on oceanic and atmospheric anomalies. **a** Depth-latitude maps of the regression coefficient for the linear regression of zonal-mean (153°–165°E) ocean temperature anomalies (°C) with the normalized KE SSH index, which is divided by one standard deviation, without lags. **b** Spatial maps of regression coefficients for the linear regression of SST (shading; °C) and 500hPa geopotential height (contours; m) anomalies on the normalized KE SSH index without lags. **c** Latitude-pressure maps of correlation coefficients between the zonal-mean (140°E–180°E) geopotential height anomalies (m) and the KE SSH index without lags. The black contours indicate regression coefficients statistically significant at the 10% level.

processes (Fig. 4). Seasonal regression maps between 3-month running mean ocean temperature and SST anomalies with the 3-month running mean KE SSH index are shown in Fig. 4a, b (e.g., the panel (JFM) indicates the JFM anomalies regressed on the JFM KE SSH index). We note that the upper (0–100 m) ocean temperature anomalies over the KE region become stronger from late spring to summer (AMJ to JJA in Fig. 4a), accompanied by warm SST anomalies over the KOE region (AMJ to JJA in Fig. 4b). The significant variations of ocean anomalies during the warm season can be supported by previous findings that the Kuroshio transport across the south of Japan (e.g., Tokara Strait) and at the upstream region has maximum in spring/summer²⁴. As the contribution of advection by the Kuroshio system becomes increasingly important in summer⁴⁵, the heat transport via horizontal advection seems to be a major contributor in affecting upper ocean temperature anomalies associated with the KE SSH. The stronger oceanic connections between the surface and subsurface in spring/summer despite increasing vertical stratification, however, are questionable and will be revisited in future studies. From Fig. 4a, b, we find that the enhanced upper ocean warm anomalies substantially increase the local KOE SST warming from AMJ to JJA, which may affect the overlying atmosphere^{46,47}.

We next show the impacts of the increase in summer KOE surface warming on anomalous atmospheric circulations (e.g.,

geopotential heights) during the KE SSH events (Fig. 4b, c). Seasonal changes in troposphere vertical motions associated with KE SSH variability are shown in Fig. 4c. We note that horizontal and vertical atmospheric anomalies associated with KE SSH show substantial changes from the spring to summer. Specifically, the barotropic vertical structure of height pressure anomalies with a north-south orientation, which was maintained in the late winter and early spring (JFM to MAM in Fig. 4b, c) and accompanied by a basin-scale SST gyre pattern (shadings of JFM to MAM in Fig. 4b), transitions into a baroclinic vertical structure with dipole anomalies tilting poleward after spring (AMJ to SON in Fig. 4c) as the local KOE SST warming becomes prominent (shadings of AMJ to JJA in Fig. 4c). We attribute the changes in geopotential height anomalies to an increase in baroclinic instability arising from the intensified cross-frontal SST gradient due to KOE surface warming, as previous studies have demonstrated^{46–52}. Studies have revealed that nonlinear dynamics, such as transient eddy vorticity fluxes, can drive an atmospheric response to extratropical SST anomalies. In particular, Smirnov et al. (2015) show that the strong upward velocity anomalies of the vertical atmospheric circulation over the warm SST anomalies enhance low-level eddy moisture fluxes and reduce the low-level stability. The increasing lower tropospheric baroclinicity shown in AMJ–SON of Fig. 4c is supported by seasonal changes in the Eady growth rate

(Supplementary Fig. 2), where the Northwestern Pacific is characterized by strong dipole anomalies from summer to autumn. It is important to note that the increasing low-level baroclinicity appears to lead the subpolar (i.e., northern) low-pressure anomalies to be displaced toward the south of the latitude 38°N, contributing to a deepening anomalous low in the lower troposphere in early winter (OND and NDJ in Fig. 4b, c). Those two cells—which in our study form a tropospheric circulation with downward (southward) flow over the south of the KOE front and upward (northward) flow over the north of the front (AMJ–SON of Fig. 4c)—are consistent with the atmospheric response to warm KOE SST anomalies reported in Smirnov et al. 2015 (see their Fig. 4c), which has been only detected in a high-resolution model. While the detailed development of those large-amplitude low-pressure anomalies during earlier winter (OND and NDJ in Fig. 4b) needs to be further diagnosed, our results show that the strong low-pressure system of OND and NDJ might be closely associated with ocean-driven changes (e.g., KOE upper-ocean temperature anomalies and related SST warming).

In this study, we suggest that the earlier winter atmospheric anomalies induced by upper-ocean KE variability play a key role in driving significant seasonal KOE air-sea heat exchanges. Consistent with Fig. 4b, Fig. 5a shows noticeable differences in the sea level pressure (SLP) patterns associated with KE SSH between the early (e.g., SON to NDJ) and late (e.g., DJF to MAM) cold seasons. From DJF to MAM, the KE SSH variability is accompanied by a basin-scale dipole SLP pattern, which resembles the North Pacific Oscillation⁵³. From SON to NDJ, on the other hand, the northern lobe of low SLP anomalies becomes deeper and shifts towards the south near the KOE downstream (as also shown in Fig. 4b), resembling the Aleutian low⁵⁴. Note that the anomalous upward heat fluxes become prominent during only the early cold season (OND, NDJ, and DJF in Fig. 5a), whereas no significant anomalies are found in any other seasons. We suggest that the 1-month preceding Aleutian-low like anomalies (SON, OND, and NDJ in Fig. 5a), which are associated with increasing baroclinicity due to warming KOE surface in Fig. 4b, c, are important to lead the significant KOE upward surface heat fluxes, via northwesterly winds that bring colder and drier air masses into the Northwestern Pacific.

To measure the ocean's physical contribution to surface heat flux anomalies, we examine the relative contributions of the anomalous wind and sea-air temperature difference (SST–SAT) to heat flux changes (Fig. 5b, c). The anomalous SHF and LHF in Fig. 5 and Supplementary Fig. 3 are estimated as bulk surface fluxes as follows.

$$\text{SHF}' = \rho c_p C_s (W \Delta T)', \text{LHF}' = \rho L C_L (W \Delta Q)' \quad (1)$$

In Eq. (1), primes indicate anomalies, ρ is the air density, c_p is the specific heat at constant pressure, C_s is the sensible heat bulk transfer coefficient, W is the scalar wind speed, ΔT is the difference of sea-air potential temperature, L is the latent heat of water vaporization, C_L is the latent heat bulk transfer coefficient, and ΔQ is the difference of specific humidity. The areal-mean SHF anomalies in the KOE region are nearly identical to the KOE SHF index of this study ($R = 0.91$ for monthly index), and so we use wind speed and SST–SAT anomalies averaged over the KOE region (25°–45°N & 135°–180°E) in the diagrams. The higher regression and correlation coefficients between SHF and SST–SAT (upper panels in Fig. 5b) than between SHF and wind speed (bottom panels in Fig. 5b) reveal that the ocean-atmosphere temperature difference dominantly controls the KOE air-sea heat exchange. The regression map of the NDJ SST (shading in Fig. 5c) and SST–SAT (contour in Fig. 5c) onto the ASO KE SSH index shows that the sea-air temperature differences are primarily characterized by the SST anomaly pattern rather than SAT anomalies (Supplementary Fig. 4), describing the SST as the critical contributor. Our results are

consistent with recent findings using a high-resolution ocean general circulation model⁴⁵, where the ocean-atmosphere temperature difference is a crucial predictor for winter variations of the net surface heat fluxes, especially the upward turbulent fluxes. The same analysis but with LHF fluxes (Supplementary Fig. 3) reveals that the SST, by controlling the saturation specific humidity at the ocean surface, also plays a more important role than the wind speed in determining the earlier winter LHF (especially in OND).

Finally, seasonal lead-lag correlations between the KE SSH and KOE heat fluxes (Fig. 6a, b) show that the KE SSH significantly leads the KOE LHF and SHF in satellite records, where the earlier cold season (e.g., OND to DJF) KOE heat fluxes are consistently led by warm season KE SSH. A lead-lag correlation of the sum of KOE SHF and LHF (Fig. 6c) shows their maximum correlations when the summer (especially ASO) KE SSH leads the earlier winter (especially NDJ) KOE heat fluxes. The substantial resemblance between the ASO KE SSH and NDJ KOE heat flux time series (Fig. 6d–f) reveals that the KOE heat flux variations effectively represent the KE SSH variability not only on decadal (Fig. 6) but also on seasonal scales (Fig. 3), explaining a substantial portion (~50%) of its total variance. Specifically, our findings show that NDJ KOE heat fluxes are critically linked to KE SSH fluctuations, which could be a key player linking the KE SSH and other Pacific climate variability that have been observed and discussed in previous studies (e.g., Pacific Decadal Precession^{28,29}, ENSO^{21,27}, and Northeast Pacific Marine Heatwaves³⁰).

DISCUSSION

Using observational satellite and reanalysis, we have examined the role of upper-ocean variations over the Kuroshio-Oyashio Extension (KOE) region in the Northwest Pacific. While previous literature has extensively focused on the low-frequency component of the KOE oceanic variations (e.g., SSH, ocean heat content, or upper-ocean temperature), the present study centers on seasonal changes in coupled ocean-atmosphere processes of those ocean decadal fluctuations. Consistent with the previous view, our findings support the view that the surface heat fluxes are key indicators of KOE decadal variations^{19,20}. We further show that earlier winter (i.e., NDJ) KOE latent (LHF) and sensible (SHF) heat fluxes are the main conveyor of decadal ocean variability to seasonal air-sea heat fluxes.

Our main findings indicate that seasonal ocean heat content anomalies associated with KE SSH variations can be a significant source of earlier winter air-sea heat exchange variations over the KOE. From spring to summer, the KOE upper ocean warm temperature anomalies associated with KE SSH become stronger. By increasing ocean surface warming and the meridional SST gradient over the Northwestern Pacific, the summer ocean temperature anomalies associated with KE SSH appear to enhance the low-level atmospheric baroclinicity, contributing to a significant transition in coupled air-sea structures. Our results, where the North-South dipole SLP pattern evolves into the large-scale monopole atmospheric circulation (e.g., Aleutian-low like pattern) from spring to fall, suggest that the anomalous ocean heat content accumulated during summer might play a role in upward KOE heat transfer during earlier winter. During summer, the relatively weaker wind speeds (i.e., weaker prevailing Northwesterly winds) and the shallower mixed layer depth might allow the subsurface ocean to accumulate contributions of anomalous ocean heat content driven by geostrophic advection (e.g., the arrival of westward propagating Rossby waves). This anomalous ocean heat content accumulated during summer might be especially important for the upward KOE heat flux anomalies during earlier winter (i.e., October-to-December), where the background wind changes are still weaker compared to the late winter (i.e., December-to-February).

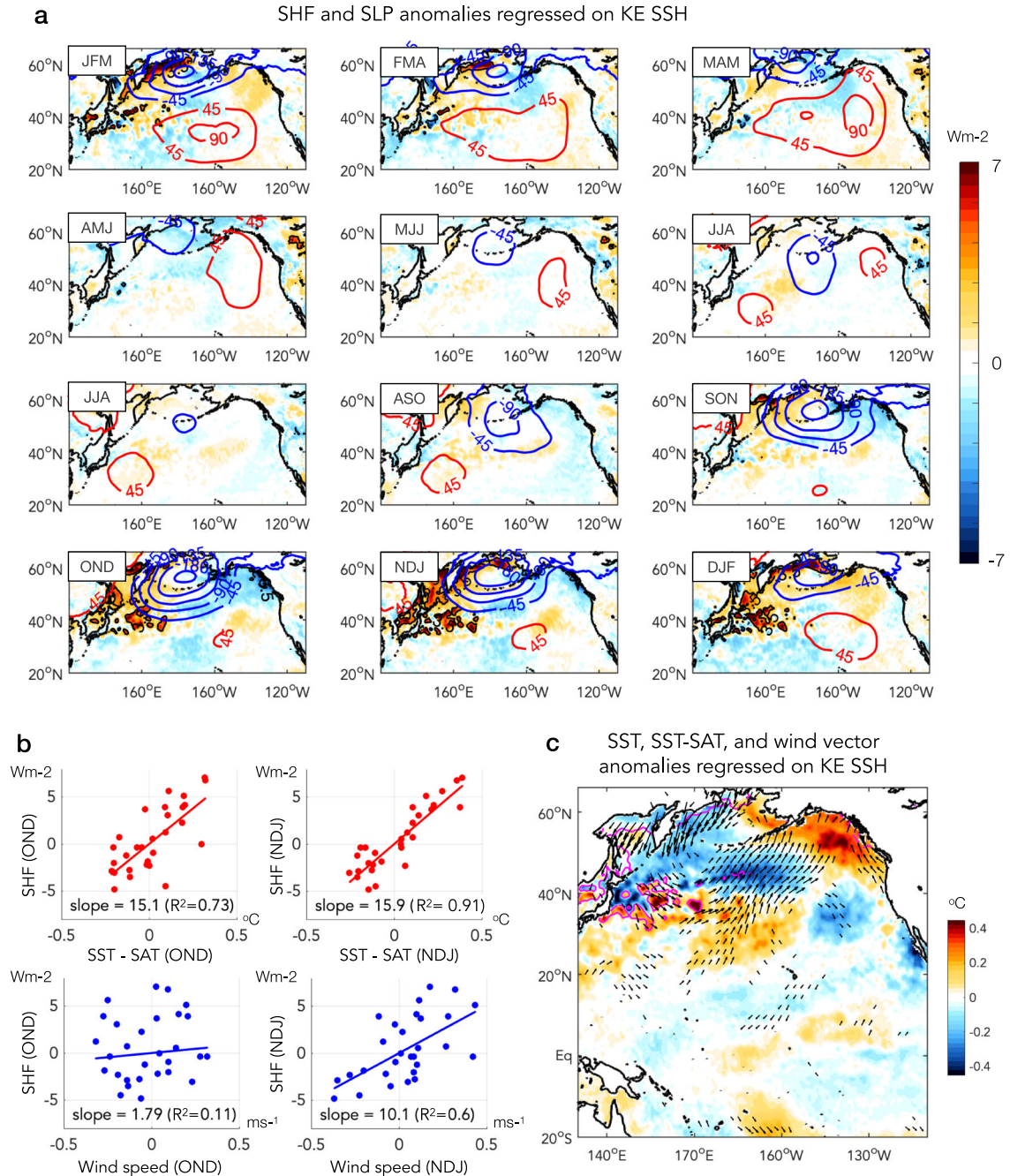


Fig. 5 Seasonal air-sea coupled patterns associated with KE SSH and quantification of KOE SHF anomalies. **a** Spatial maps of regression coefficients for the linear regression of surface LHF (shading; Wm^{-2}) and SLP (contours; Pa) anomalies on the normalized KE SSH index, divided by one standard deviation, without lags. **b** Scatterplots of areal indices of SHF vs. sea-air temperature difference (SST-SAT; $^{\circ}\text{C}$) in the top panels and SHF vs. wind speed (ms^{-1}) anomalies in the bottom panels over the KOE region (25° – 45°N and 135° – 180°E). OND (left panels) and NDJ (right panel) time series are used. The straight line is the least squares linear fit to the plotted points; the regression coefficient (slope; $\text{Wm}^{-2}/^{\circ}\text{C}$ for top and $\text{Wm}^{-2}/\text{ms}^{-1}$ for bottom) and squared correlation coefficient (r^2) are labeled in each plot. **c** Maps of regression coefficients for the linear regression of NDJ SST (shading; $^{\circ}\text{C}$), SST-SAT (magenta contour; 0.19°C), and wind vector (m/s) anomalies onto the normalized ASO KE SSH index. Wind vectors that are significant at the 10% level are shown.

While the recent study by Gan et al. 2023⁵⁵ shows that subseasonal variations of climatological background wind likely drive subseasonal changes of KOE air-sea heat flux anomalies, our composite analysis (Supplementary Fig. 5) indicates that the role of background wind climatology in the earlier winter response of SSH-related KOE heat fluxes might be less critical. In Supplementary Fig. 5, the background wind changes (red contours) are most prominent from November to March and peak in January. The KOE

heat flux anomalies during neutral years thus seem to respond to the intense background wind intensity, showing the largest LHF response during later winter (from January to March; blue boxes of upper panels). However, during strong positive KE SSH years, the most significant KOE LHF anomalies are observed during earlier winter (from October to December; red boxes of bottom panels), supporting Fig. 5a. In addition, while several studies have suggested significant subseasonal variations of air-sea heat flux

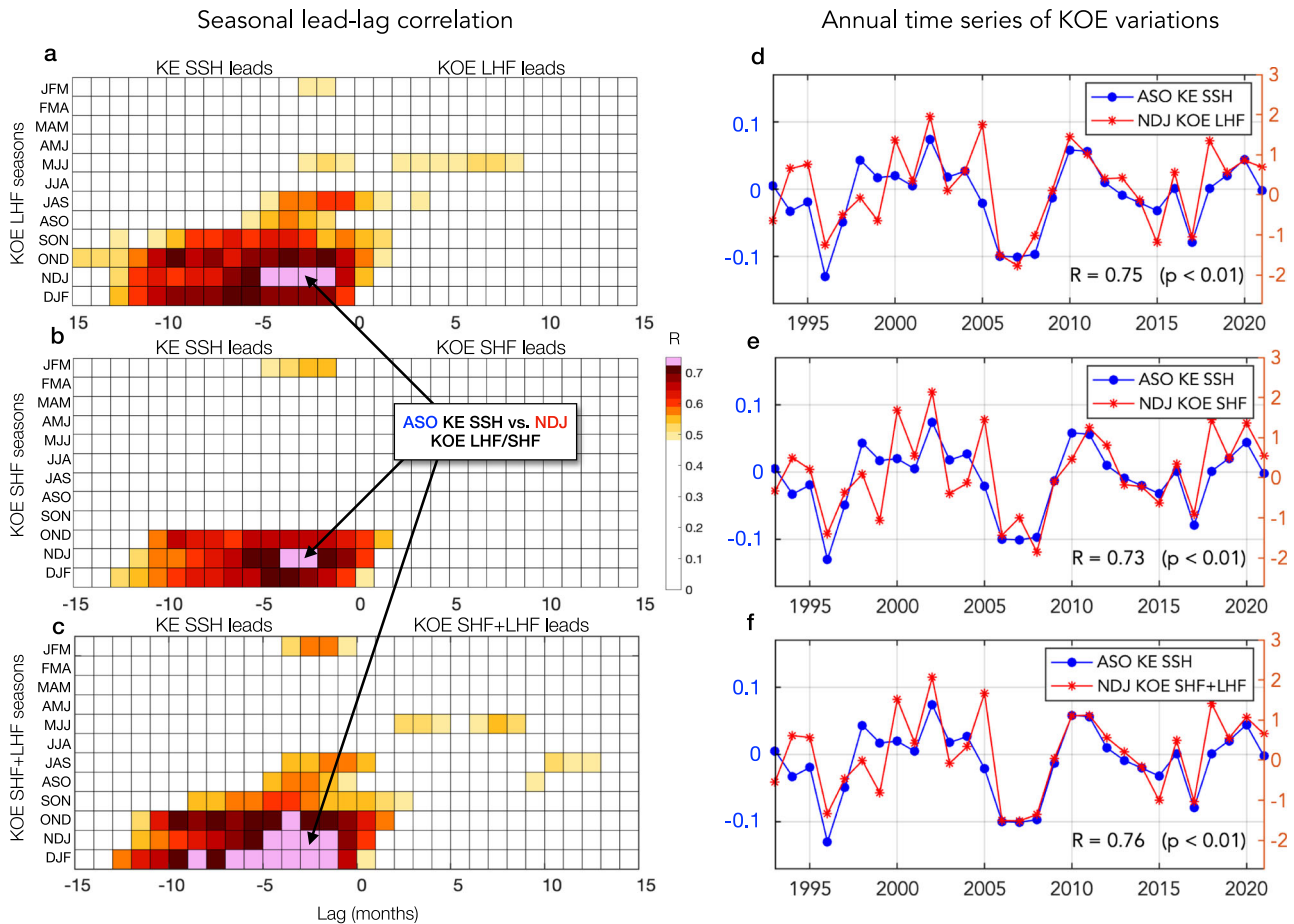


Fig. 6 Seasonal covariability between KE SSH and KOE heat fluxes. **a** Lead-lag correlation between 3-month running mean KE SSH and KOE LHF. Only correlation coefficients that are significant at the 5% level are shaded, where the adjusted degrees of freedom are ~ 14 for two-tail tests. The y-axis label indicates the season of the KOE LHF at increments of 1 month, and the x-axis label indicates the lag in months between the KE SSH and KOE LHF, where negative lags indicate that KE SSH leads the KOE LHF, and the reverse holds for positive lags. For example, the coordinate $(-3, \text{NDJ})$ (i.e., where the top arrow points) indicates where the NDJ KOE LHF is led by ASO KE SSH by 3 months. **b** Same as in **(a)** but for the SHF. **c** Same as in **(a)** but for the SHF + LHF. **d** Seasonal time series of August–September–October (ASO) KE SSH and November–December–January (NDJ) KOE LHF, where they show the maximum correlation in the seasonal lead-lag correlation. **e** Same as in **(b)** but for the SHF. **f** Same as in **(b)** but for the SHF + LHF.

anomalies over the KOE^{17,55}, our findings indicate that there is a strong consistency between seasonal (e.g., 3-month-mean; Fig. 4b) and subseasonal (e.g., monthly; Supplementary Fig. 6) variations of SST and SLP anomalies associated with KE SSH. The close quantification of impacts of background state and ocean dynamics on air-sea turbulent heat exchanges over the KOE on subseasonal time scales might need to be revisited. Collectively, our results suggest that the summer KE SSH anomalies could be a critical component of predictability for the North Pacific seasonal air-sea coupled processes of earlier winter. The quantified oceanic and atmospheric components of earlier winter KOE surface heat fluxes show that the ocean-driven SST anomalies play a prime role in determining the ocean-atmosphere temperature difference, strengthening the anomalous heat transfer from the ocean to the atmosphere.

One of the merits of using the surface heat fluxes is that they can hint at slowly-evolving subsurface variations that are currently constrained by satellite observations (e.g., SSH) or Argo (e.g., ocean temperature). Given that the spatial patterns of KOE LHF/SHF associated with KE SSH are characterized by *quasi-stationary* meanders related to the geographical location, we use projections of those patterns and extend their time series back to 1959 (see method for more details). The stationary spatial patterns of the KOE heat flux variability over >60 years in the observational

records (i.e., 1959–2022) are confirmed in empirical orthogonal function (EOF) analysis of KOE LHF anomalies (Supplementary Fig. 7), where the constructed KOE heat flux indices in this study (Fig. 7a) highly correspond to the most dominant variability (e.g., the leading EOF mode). Two-year running mean KOE LHF/SHF indices for the extended period in Fig. 7a exhibit that the covariation of LHF and SHF and their low-frequency components have noticeably increased since 1990. We attribute the increasing correlation of those two-year running mean KOE LHF and KOE SHF from 0.31 (before 1990) to 0.86 (after 1990) to their enhanced low-frequency covariability because the correlation of monthly indices between KOE LHF and KOE SHF has barely changed from before ($R = 0.72$) to after ($R = 0.75$) 1990. We note that both the low-pass filtered KOE LHF and SHF variations have a prominent quasi-decadal spectral peak (e.g., 8–12 years; Fig. 7b) that is identical to the dominant time scale of the KE SSH^{2,21,22,56}. In particular, we detect a significant increase in the decadal variance (e.g., ~ 10 -year-period) of KOE heat fluxes since the mid-1980 in wavelet analysis of 2-year-running-mean KOE heat flux indices (Fig. 7c, d), which is confirmed both in the constructed indices of KOE LHF/SHF and the leading principal components of KOE heat fluxes.

Consistent with our results that the decadal KOE heat flux variations are mainly driven by earlier winter air-sea heat exchange, the enhanced decadal fluctuations seem to be due to

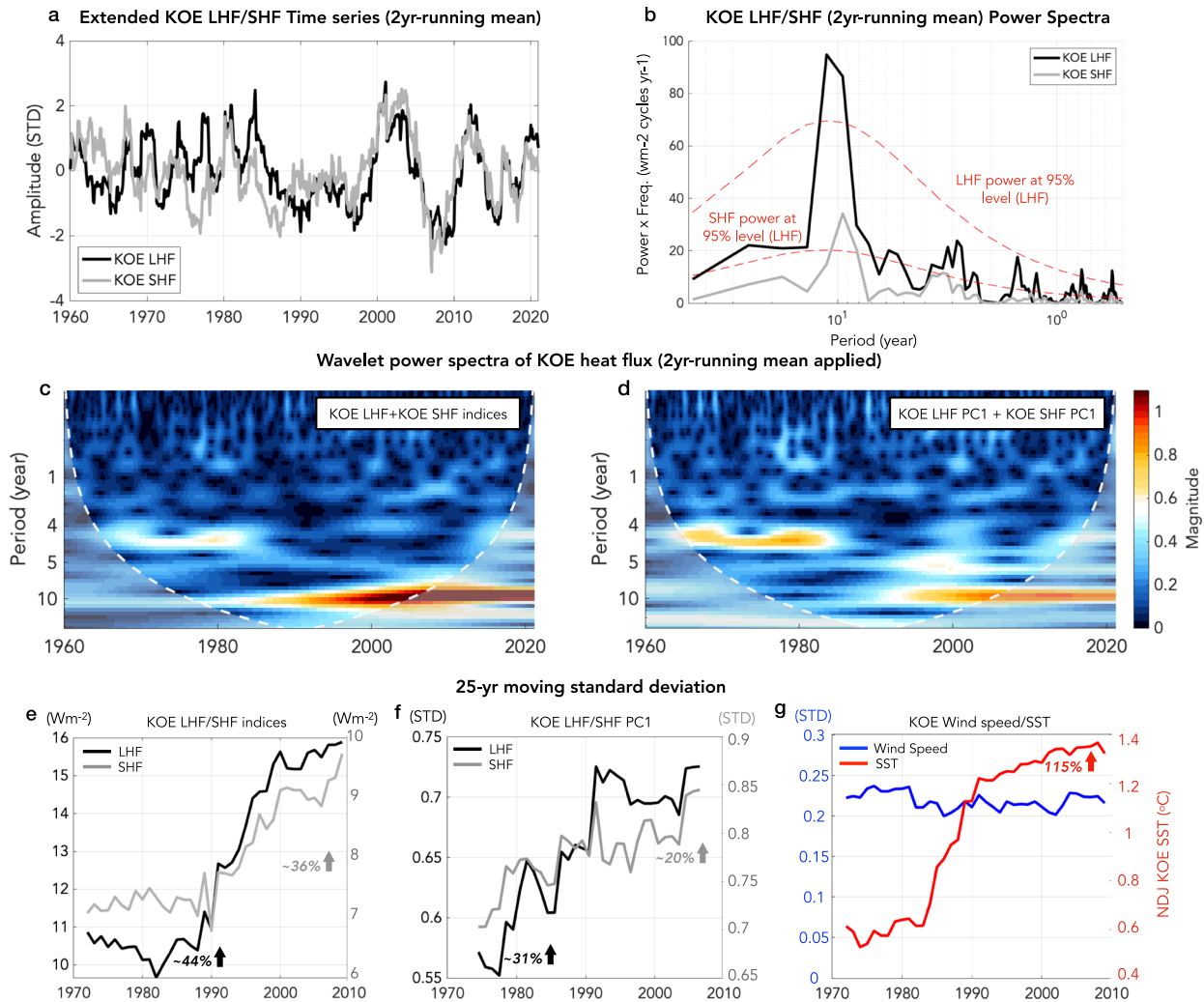


Fig. 7 KOE heat fluxes as a decadal climate indicator of Pacific climate and the increasing role of ocean variability in the observation record. **a** Extended time series of 2-year running mean KOE LHF/SHF associated with the KOE LHF/SHF patterns in Fig. 2a and d. **b** Power spectra of 2-year running mean KOE LHF (black) and SHF (gray) for the period between 1959 and 2021. The red dashed lines indicate the 95% significance level (higher line for LHF and lower line for SHF). **c** Wavelet power spectra of the sum of KOE LHF and KOE SHF indices. **d** Same as (c) but for the sum of KOE LHF PC1 and KOE SHF PC1. In **c**, **d**, the continuous wavelet transform is computed and shown by MATLAB function named “*cwtfilterbank*”. The filter bank uses approximately 10 wavelet bandpass filters per octave (10 voices per octave). **e** 25-year moving standard deviation NDJ KOE LHF and SHF indices for the period between 1959–2021. **f** Same as (e) but for NDJ KOE LHF PC1 and SHF PC1. **g** Same as (e) but for NDJ KOE wind speed and SST.

increasing variance of KOE LHF/SHF in OND and NDJ (Fig. 7e, f). It is important to note that increases in the seasonal variance of KOE LHF/SHF are detected only in the early cold season (i.e., OND and NDJ, Supplementary Fig. 8). We finally suggest that the increase in KOE heat flux variability in earlier winter can be mainly attributed to the enhanced oceanic variability (e.g., KOE SST) rather than atmospheric variance (e.g., wind speed) in Fig. 7g. All those increases in KOE variances exceeding ~35% shown in Fig. 7e and g are highly significant ($p < 0.01$) based on a statistical significance test using the Monte Carlo approach (see method for details). The less significant increasing variance (Fig. 7f) of the leading time series of KOE LHF/SHF EOF might be due to strong stochastic components included in the dominant mode of surface heat fluxes. The observed changes in KOE variations in this study are consistent with recent observational and modeling studies that report significant changes in variance and time scale of the KE SSH, such as the stronger decadal KE variability during the recent period and under simulated future climate change^{27,57–59}. Those observed and projected enhanced decadal ocean variations in a warming climate suggest that the changes in earlier winter heat

transport over the KOE might be a response to increasing anthropogenic forcing. However, without climate model experiments/projections and further analysis, we do not conclude that the increasing variance of KOE heat fluxes is solely due to external forcing because of the possibility of much lower frequency modulations (e.g., centennial time scales) of oceanic variations. Our study suggests that the increasing role of both physical (e.g., SSH) and thermodynamical (e.g., LHF/SHF) variations over the KOE region can be a key component of understanding the Pacific ocean-atmosphere coupled system as the conveyor of decadal ocean variability to air-sea coupling.

Given the increasing ocean-atmosphere coupled processes over the Northwestern Pacific on both seasonal and decadal timescales, one important and challenging question is how we can apply our findings and understandings to current climate predictions and climate change. Could the North Pacific WBC variations be important sources of seasonal-to-decadal climate predictability and change, especially for the Asia-Pacific-North America sector and variables? Further investigation of variations and changes in WBC thermal impact on midlatitude weather and climate,

including hydrological cycles and extreme events, will be essential for real-time predictions and support for climate adaptation and mitigation.

METHODS

Observational datasets

We use satellite SSH from the Copernicus Marine and Environment Monitoring Service (CMEMS), which has merged along-track satellite altimetry measurements since 1993 with a 1/12° resolution. We use subsurface ocean temperatures from a reanalysis obtained from EN4 quality-controlled dataset⁶⁰ provided by Met Office Hadley Centre. To examine SST and atmospheric fields associated with KOE ocean variations, we use surface latent and sensible heat fluxes, sea level pressure, surface air temperature, 10 m zonal and meridional winds, and 10 m wind speed, which are taken from the European Centre for Medium-Range Weather Forecasts Reanalysis-5 (ERA5)⁶¹, available on regular 0.25° grids from January 1959 onward. Surface latent and sensible heat fluxes, which are the main variables in this study, are compared to real-time in situ observations at the KEO mooring site (fixed at 32.3°N & 144.6°E) from Ocean Climate Stations project office of NOAA/Pacific Marine Environmental Laboratory (Supplementary Fig. 9). All fields are obtained as monthly datasets (except for daily mooring data), and we use both monthly and seasonal mean (i.e., 3-month mean) to show decadal and seasonal evolutions of KOE variations, respectively. Monthly anomalies are computed by subtracting the climatological monthly means and the long-term linear trend using a least square method.

Removing tropical variability

Given the strong influence of tropical Pacific variability (e.g., ENSO) on midlatitude air-sea interaction, many previous studies of the North Pacific have attempted to remove tropical SST signals from the time series at all midlatitude grid points^{2,62–64}. Following their approach, we apply and remove linear regressions onto the concurrent and lagged (1–3 month) ENSO signals from all the atmospheric and SST anomaly fields and WBC indices (e.g., KE SSH and KOE LHF/SHF time series) prior to analysis. The ENSO signal here is defined as the first three principal components of SST anomalies in the tropical Pacific between 12.5°S and 12.5°N following Frankignoul and Sennéchal⁶⁴ (Supplementary Fig. 10). For example, each monthly anomaly at given longitude and latitude point $X(t)$ is replaced by $X(t) - aE_1(t - \tau) - bE_2(t - \tau) - cE_3(t - \tau)$, where $E_1(t)$, $E_2(t)$, and $E_3(t)$ are those first three principal components of the tropical Pacific SST anomalies, τ indicates 0–3 months considering delayed response of atmospheric ENSO teleconnections, and a , b , and c are seasonally varying regression coefficients determined by least square fit for each variable at the grid point. The first mode (60% of the total variance) represents the traditional ENSO pattern, which is the tropical SST pattern regressed on Niño3.4 SST. The second mode (13.2% of the variance) represents the dipole SST contrast (i.e., east-west), and the third (4.4% of the variance) exhibits a narrow SST signature along the equator.

Definition of KE SSH and KOE LHF and SHF indices

We adopt an index of KE SSH variability introduced by Qiu et al. (2014)¹⁵, in which KE SSH variability is defined as the SSH anomalies averaged over the KE region [31°–36°N, 140°–165°E]. This index effectively describes dynamic properties of the Pacific WBC system, such as the latitude of the oceanic front and eastward jet, intensity of the KE recirculation gyre, and ocean heat content^{9,15,33,38}. Spatial patterns of the KOE surface latent heat flux (LHF) and sensible heat flux (SHF) associated with the KE SSH are identified by regressing 3-month lagged LHF and SHF onto the KE

SSH index. The 3-month lag is chosen based on the peak regression amplitude of lagged LHF/SHF anomalies regressed onto the KE SSH index (Fig. 2). The regressed patterns of LHF and SHF anomalies over the KOE region (25°–45°N & 135°–180°E) appear to show distinct geographical characteristics (e.g., quasi-stationary meanders of the upstream KE [140°–153°E & 31°–36°N]⁹). To obtain the corresponding KOE LHF/SHF time-series, we project the spatial patterns of the KOE LHF and SHF onto monthly LHF and SHF anomalies, respectively, following Zhao and Di Lorenzo (2020)⁶⁵ who identify patterns and indices of ENSO precursor (note that we avoid using box-averages of KOE heat fluxes in order to detect geographical features and exclude unrelated intrinsic air-sea coupled processes). The domain for calculating the projections is the KOE region over the North-western Pacific (25°–45°N & 140°E–180°W). The KOE SST time series is obtained with the same projection method but with the larger projection region, which covers the whole North Pacific (20°–60°N & 120°E–110°W), in order to include the basin-scale SST signature associated with KE SSHa (e.g., North-South phase dipole SST anomalies). The KE SSH and KOE LHF and SHF indices are initially computed with monthly data, and their seasonal indices are obtained by using 3-month running means.

Adjusted degrees of freedom

To conduct the significance test for correlations of decadal time scale and low-pass filtered climate indices (e.g., KE SSH index or 2 year-running mean time series), where the autocorrelation time scales are longer than ~1.5 years, we use adjusted degrees of freedom following Bretherton et al. (1999)⁶⁶:

$$N^* = \frac{N}{1 + 2 \sum_{j=1}^{N-1} (1 - \frac{j}{N}) \rho_{xx}(j) \rho_{yy}(j)}$$

where N is the number of time steps, and $\rho_{xx}(j)$ and $\rho_{yy}(j)$ are the autocorrelation coefficient of time series x and y at lag j . Statistical significance tests using adjusted degrees of freedom have been widely used for investigation and assessment of low-frequency climate variations^{67,68}.

Monte Carlo significance test

In this study, we show noticeable long-term changes in the earlier winter KOE variability for the extended observational record (i.e., 1959–2021). To determine if those annual changes (e.g., increasing/decreasing linear slope) are statistically significant, we use the Monte Carlo significance test with 30,000 random time series that contain the same number of time steps, mean, standard deviation, and autocorrelation as the observed KOE indices, via a first-order autoregressive model with no long-term trend. Using the obtained p -value based on distributions of slope changes of random sample variances, we determine the significance level that can reject a null hypothesis, which assumes that there are no changes in the linear slope (i.e., no long-term trends). For each synthetic time series, the running standard deviation is computed, along with the linear trend of that running standard deviation. The Monte Carlo sample percentiles of these trends provide tail probabilities for the null hypothesis of no forced trend, against which the observed trends can be compared.

DATA AVAILABILITY

The merged satellite altimeter data were obtained from SSALTO/DUACS and the Copernicus Marine and Environment Monitoring Service (<https://data.marine.copernicus.eu/products>). EN4 data was obtained from <https://www.metoffice.gov.uk/hadobs/en4/>. The ERA5 datasets were taken from <https://cds.climate.copernicus.eu/#/search?text=ERA5&type=dataset>. The real-time KEO mooring data was obtained from NOAA PMEL Ocean Climate Station (<https://www.pmel.noaa.gov/ocs/data/disdell/>).

CODE AVAILABILITY

Codes generated by this present study are available from the corresponding author upon request.

Received: 1 April 2023; Accepted: 11 August 2023;
Published online: 22 August 2023

REFERENCES

- Schneider, N. & Cornuelle, B. D. The forcing of the Pacific decadal oscillation. *J. Clim.* **18**, 4355–4373 (2005).
- Qiu, B., Schneider, N. & Chen, S. Coupled decadal variability in the North Pacific: an observationally constrained idealized model. *J. Clim.* **20**, 3602–3620 (2007).
- Kwon, Y.-O. & Deser, C. North Pacific decadal variability in the community climate system model version 2. *J. Clim.* **20**, 2416–2433 (2007).
- Taguchi, B. et al. Decadal variability of the Kuroshio extension: observations and an Eddy-resolving model hindcast*. *J. Clim.* **20**, 2357–2377 (2007).
- Nonaka, M., Nakamura, H., Tanimoto, Y., Kagimoto, T. & Sasaki, H. Decadal variability in the Kuroshio–Oyashio extension simulated in an Eddy-resolving OGCM. *J. Clim.* **19**, 1970–1989 (2006).
- Na, H., Kim, K.-Y., Minobe, S. & Sasaki, Y. N. Interannual to decadal variability of the upper-ocean heat content in the Western North Pacific and its relationship to oceanic and atmospheric variability. *J. Clim.* **31**, 5107–5125 (2018).
- Wu, B., Lin, X. & Yu, L. Poleward shift of the Kuroshio extension front and its impact on the North Pacific subtropical mode water in the recent decades. *J. Phys. Oceanogr.* **51**, 457–474 (2021).
- Qiu, B. Interannual variability of the Kuroshio Extension system and its impact on the wintertime SST field. *J. Phys. Oceanogr.* **30**, 1486–1502 (2000).
- Qiu, B. & Chen, S. Variability of the Kuroshio Extension Jet, recirculation gyre, and mesoscale eddies on decadal time scales. *J. Phys. Oceanogr.* **35**, 2090–2103 (2005).
- Xie, S.-P. et al. Global warming pattern formation: sea surface temperature and rainfall*. *J. Clim.* **23**, 966–986 (2010).
- Nonaka, M., Nakamura, H., Tanimoto, Y., Kagimoto, T. & Sasaki, H. Interannual-to-decadal variability in the oyashio and its influence on temperature in the sub-arctic frontal zone: an eddy-resolving OGCM simulation. *J. Clim.* **21**, 6283–6303 (2008).
- Seager, R., Kushnir, Y., Naik, N. H., Cane, M. A. & Miller, J. Wind-driven shifts in the latitude of the Kuroshio–Oyashio Extension and generation of SST anomalies on decadal timescales. *J. Clim.* **14**, 4249–4265 (2001).
- Joyce, T. M., Kwon, Y.-O. & Yu, L. On the relationship between synoptic wintertime atmospheric variability and path shifts in the gulf stream and the Kuroshio Extension. *J. Clim.* **22**, 3177–3192 (2009).
- Frankignoul, C., Sennéchal, N., Kwon, Y.-O. & Alexander, M. A. Influence of the meridional shifts of the Kuroshio and the oyashio extensions on the atmospheric circulation. *J. Clim.* **24**, 762–777 (2011).
- Qiu, B., Chen, S., Schneider, N. & Taguchi, B. A coupled decadal prediction of the dynamic state of the Kuroshio extension system. *J. Clim.* **27**, 1751–1764 (2014).
- Minobe, S., Miyashita, M., Kuwano-Yoshida, A., Tokinaga, H. & Xie, S.-P. Atmospheric response to the gulf stream: seasonal variations*. *J. Clim.* **23**, 3699–3719 (2010).
- Taguchi, B. et al. Seasonal evolutions of atmospheric response to decadal SST anomalies in the North Pacific subarctic frontal zone: observations and a coupled model simulation. *J. Clim.* **25**, 111–139 (2012).
- Kelly, K. A. et al. Western boundary currents and frontal Air–Sea interaction: Gulf stream and Kuroshio extension. *J. Clim.* **23**, 5644–5667 (2010).
- Schneider, N. & Miller, A. J. Predicting Western North Pacific Ocean climate. *J. Clim.* **14**, 3997–4002 (2001).
- Schneider, N., Miller, A. J. & Pierce, D. W. Anatomy of North Pacific decadal variability. *J. Clim.* **15**, 586–605 (2002).
- Joh, Y. & Di Lorenzo, E. Interactions between Kuroshio extension and central Tropical Pacific lead to preferred decadal-timescale oscillations in Pacific climate. *Sci. Rep.* **9**, 13558 (2019).
- Anderson, B. T. Empirical evidence linking the Pacific decadal precession to Kuroshio extension variability. *J. Geophys Res-Atmos.* **124**, 12845–12863 (2019).
- Siqueira, L., Kirtman, B. P. & Laurindo, L. C. Forecasting remote atmospheric responses to decadal Kuroshio stability transitions. *J. Clim.* **34**, 379–395 (2021).
- Qiu, B. Kuroshio and Oyashio currents. *Ency. Ocean Sci.* **3**, 382–394 (2019).
- Ceballos, L. I., Di Lorenzo, E., Hoyos, C. D., Schneider, N. & Taguchi, B. North Pacific Gyre oscillation synchronizes climate fluctuations in the eastern and western boundary systems. *J. Clim.* **22**, 5163–5174 (2009).
- Qiu, B. & Chen, S. Eddy-mean flow interaction in the decadal modulating Kuroshio Extension system. *Deep Sea Res. II: Top. Stud. Oceanogr.* **57**, 1098–1110 (2010).
- Joh, Y., Di Lorenzo, E., Siqueira, L. & Kirtman, B. P. Enhanced interactions of Kuroshio Extension with tropical Pacific in a changing climate. *Sci. Rep.* **11**, 6247 (2021).
- Anderson, B. T., Gianotti, D. J. S., Salvucci, G. & Furtado, J. Dominant time scales of potentially predictable precipitation variations across the continental United States. *J. Clim.* **29**, 8881–8897 (2016).
- Anderson, B. T., Gianotti, D. J. S., Furtado, J. C. & Di Lorenzo, E. A decadal precession of atmospheric pressures over the North Pacific. *Geophys. Res. Lett.* **43**, 3921–3927 (2016).
- Capotondi, A., Newman, M., Xu, T. & Di Lorenzo, E. An optimal precursor of Northeast Pacific Marine heatwaves and Central Pacific El Niño events. *Geophys. Res. Lett.* **49**, e2021GL097350 (2022).
- Tourre, Y. M., Kushnir, Y. & White, W. B. Evolution of interdecadal variability in sea level pressure, sea surface temperature, and upper ocean temperature over the Pacific ocean. *J. Phys. Oceanogr.* **29**, 1528–1541 (1999).
- Vivier, F., Kelly, K. A. & Thompson, L. A. Heat budget in the Kuroshio extension region: 1993–99. *J. Phys. Oceanogr.* **32**, 3436–3454 (2002).
- Kelly, K. A. The relationship between oceanic heat transport and surface fluxes in the Western North Pacific: 1970–2000. *J. Clim.* **17**, 573–588 (2004).
- Kelly, K. A. & Dong, S. *The Relationship of Western Boundary Current Heat Transport and Storage to Mid-latitude Ocean–atmosphere Interaction.* <https://agupubs.onlinelibrary.wiley.com/doi/10.1029/147GM19> (2004).
- Taguchi, B., Schneider, N., Nonaka, M. & Sasaki, H. Decadal variability of upper-ocean heat content associated with meridional shifts of Western Boundary current extensions in the North Pacific. *J. Clim.* **30**, 6247–6264 (2017).
- Ma, X. et al. Distant influence of Kuroshio eddies on North Pacific weather patterns? *Sci. Rep.* **5**, 17785 (2015).
- Ma, X. et al. Importance of resolving Kuroshio front and eddy influence in simulating the North Pacific storm track. *J. Clim.* **30**, 1861–1880 (2017).
- Qiu, B. The Kuroshio Extension system: its large-scale variability and role in the midlatitude ocean–atmosphere interaction. *J. Phys. Oceanogr.* **58**, 57–75 (2002).
- Latif, M. & Barnett, T. P. Causes of decadal climate variability over the North Pacific and North America. *Sci* **266**, 634–637 (1994).
- Miller, A. J., Cayan, D. R. & White, W. B. A westward-intensified decadal change in the North Pacific thermocline and gyre-scale circulation. *J. Clim.* **11**, 3112–3127 (1998).
- Schneider, N., Miller, A. J., Alexander, M. A. & Deser, C. Subduction of Decadal North Pacific temperature anomalies: observations and dynamics. *J. Phys. Oceanogr.* **29**, 1056–1070 (1999).
- Qiu, B. Kuroshio extension variability and forcing of the Pacific decadal oscillations: responses and potential feedback. *J. Phys. Oceanogr.* **33**, 2465–2482 (2003).
- Qiu, B. & Kelly, K. A. Upper-ocean Heat balance in the Kuroshio extension region. *J. Phys. Oceanogr.* **23**, 2027–2041 (1993).
- Tozuka, T., Toyoda, T. & Cronin, M. F. Role of mixed layer depth in Kuroshio extension decadal variability. *Geophys. Res. Lett.* **50**, e2022GL101846 (2023).
- Pak, G. et al. Upper-ocean thermal variability controlled by ocean dynamics in the Kuroshio–Oyashio Extension region. *J. Geophys. Res: Oceans* **122**, 1154–1176 (2017).
- Nakamura, H., Sampe, T., Tanimoto, Y. & Shimpo, A. Observed associations among storm tracks, jet streams and midlatitude oceanic fronts. *Earth's Clim.* **147**, 329–345 (2004).
- Nakamura, H. & Shimpo, A. Seasonal variations in the Southern Hemisphere storm tracks and jet streams as revealed in a reanalysis dataset. *J. Clim.* **17**, 1828–1844 (2004).
- Lindzen, R. S. & Farrell, B. A simple approximate result for the maximum growth rate of baroclinic instabilities. *J. Atmos. Sci.* **37**, 1648–1654 (1980).
- Nonaka, M. et al. Air–sea heat exchanges characteristic to a prominent mid-latitude oceanic front in the South Indian Ocean as simulated in a high-resolution coupled GCM. *J. Clim.* **22**, 6515–6535 (2009).
- Hotta, D. & Nakamura, H. On the significance of sensible heat supply from the ocean in the maintenance of mean baroclinicity along storm tracks. *J. Clim.* **24**, 3377–3401 (2011).
- Nakayama, M., Nakamura, H. & Ogawa, F. Impacts of a midlatitude oceanic frontal zone for the baroclinic annular mode in the Southern Hemisphere. *J. Clim.* **34**, 7389–7408 (2021).
- Seo, H. et al. Ocean mesoscale and frontal-scale Ocean–atmosphere interactions and influence on large-scale climate: a review. *J. Clim.* **36**, 1981–2013 (2023).
- Baxter, S. & Nigam, S. Key role of the North Pacific Oscillation–West Pacific pattern in generating the extreme 2013/14 North American Winter. *J. Clim.* **28**, 8109–8117 (2015).
- Trenberth, K. E. & Hurrell, J. W. Decadal atmosphere–ocean variations in the Pacific. *Clim. Dyn.* **9**, 303–319 (1994).
- Gan, B. et al. A mesoscale Ocean–Atmosphere coupled pathway for decadal variability of the Kuroshio extension system. *J. Clim.* **36**, 485–510 (2023).

56. Joh, Y. & Di Lorenzo, E. Increasing coupling between NPGO and PDO leads to prolonged Marine Heatwaves in the Northeast Pacific. *Geophys. Res. Lett.* **44**, 663–611,671 (2017).
57. Sun, J. et al. Impacts of the interannual variability of the Kuroshio extension on the East Asian trough in winter. *Atmos* **13**, 996 (2022).
58. Wang, Y.-H. & Liu, W. T. Observational evidence of frontal-scale atmospheric responses to Kuroshio Extension variability. *J. Clim.* **28**, 9459–9472 (2015).
59. Joh, Y. et al. Stronger decadal variability of the Kuroshio Extension under simulated future climate change. *npj Clim. Atmos. Sci.* **5**, 63 (2022).
60. Good, S. A., Martin, M. J. & Rayner, N. A. EN4: Quality controlled ocean temperature and salinity profiles and monthly objective analyses with uncertainty estimates. *J. Geophys. Res.: Oceans* **118**, 6704–6716 (2013).
61. Hersbach, H. et al. The ERA5 global reanalysis. *Q. J. R. Meteorol.* **146**, 1999–2049 (2020).
62. Liu, Q., Wen, N. & Liu, Z. An observational study of the impact of the North Pacific SST on the atmosphere. *Geophys. Res. Lett.* **33**, L18611 (2006).
63. Deser, C. et al. Insights from Earth system model initial-condition large ensembles and future prospects. *Nat. Clim. Change* **10**, 277–286 (2020).
64. Frankignoul, C. & Sennéchaël, N. Observed influence of North Pacific SST anomalies on the atmospheric circulation. *J. Clim.* **20**, 592–606 (2007).
65. Zhao, Y. & Di Lorenzo, E. The impacts of Extra-tropical ENSO Precursors on Tropical Pacific Decadal-scale Variability. *Sci. Rep.* **10**, 3031 (2020).
66. Bretherton, C. S., Widmann, M., Dymnikov, V. P., Wallace, J. M. & Bladé, I. The effective number of spatial degrees of freedom of a time-varying field. *J. Clim.* **12**, 1990–2009 (1999).
67. Chang, C.-C. & Wang, Z. Multiyear hybrid prediction of Atlantic tropical cyclone activity and the predictability sources. *J. Clim.* **33**, 2263–2279 (2020).
68. Yang, X. et al. On the development of GFDL's Decadal prediction system: initialization approaches and retrospective forecast assessment. *J. Adv. Mod. Ear. Sys.* **13**, e2021MS002529 (2021).

ACKNOWLEDGEMENTS

We thank Drs. Hyung-gyu Lim and Mingyu Park for constructive comments on an earlier version of the manuscript. Youngji Joh received award NA18OAR4320123 under Cooperative Institute for Modeling the Earth System (CIMES) at Princeton University and the National Oceanic and Atmospheric Administration, U.S. Department of Commerce.

AUTHOR CONTRIBUTIONS

Y.J. conceived the study and conducted the model output analysis, plotted figures, and wrote the paper. All authors contributed to interpreting the results and enhancing discussions and helped to improve the manuscript.

COMPETING INTERESTS

The authors declare no competing interests.

ADDITIONAL INFORMATION

Supplementary information The online version contains supplementary material available at <https://doi.org/10.1038/s41612-023-00453-9>.

Correspondence and requests for materials should be addressed to Youngji Joh.

Reprints and permission information is available at <http://www.nature.com/reprints>

Publisher's note Springer Nature remains neutral with regard to jurisdictional claims in published maps and institutional affiliations.



Open Access This article is licensed under a Creative Commons Attribution 4.0 International License, which permits use, sharing, adaptation, distribution and reproduction in any medium or format, as long as you give appropriate credit to the original author(s) and the source, provide a link to the Creative Commons license, and indicate if changes were made. The images or other third party material in this article are included in the article's Creative Commons license, unless indicated otherwise in a credit line to the material. If material is not included in the article's Creative Commons license and your intended use is not permitted by statutory regulation or exceeds the permitted use, you will need to obtain permission directly from the copyright holder. To view a copy of this license, visit <http://creativecommons.org/licenses/by/4.0/>.

© The Author(s) 2023